LUND UNIVERSITY

Representation of non-local optical potentials for nuclear reactions

Author: Lukas Nord

Thesis submitted for the degree of
Bachelor of Science, 15 hp
Supervisor: Andrea Idini
Examiner: Marcus Dahlström

Department of Physics
Division of Mathematical Physics
May 2024

Abstract

A scattering process is the event where particles collide with each other and then move away from each other, in any direction. This is the foundation of any reaction between nuclei and is a central part of nuclear physics.

In modelling these reactions, it is central to determine an effective potential, representing the reaction, to use in analysis. This potential is a complex potential referred to as an optical potential. There are two main approaches in determining it, the phenomenological and microscopic approach.

The phenomenological approach fits experimental data to a model to determine the optical potential while the microscopic model instead calculates it from microscopic nuclear structure and reactions. The latter is an essential for nuclei with insufficient experimental data available. It is however difficult to construct microscopic models that have the performance of phenomenological ones. The microscopic models are numerical, making them harder to give some intuitive interpretation of nuclear reactions.

This thesis takes a step towards bridging the gap between phenomenological model potentials and microscopic model potentials. Through comparative analysis, various models are projected onto one another, revealing the general shape of the microscopic model. It is then represented in an analytical form by developing an approximation of a basis for the L^2 Hilbert space that the microscopic model potential spans and then projecting the potential onto components of this basis.

The result obtained from this is the general shape of the microscopic model potential investigated. It is found to be represented by a linear combination of the Wood-Saxon and Gaussian distributions and their derivatives.

Abbreviations

KD: Koning Delaroche

SCGF: Self Consistent Greens Function theory

PB: Perey-Buck

WS: Wood-Saxon

SA-NCSM Symmetry-Adapted No-Core Shell Model

Contents

1 Introduction

Nuclear reactions are a driving force to many events in the Universe such as nucleosynthesis, fusion and fission. Understanding them would propel the scientific development forward in various fields of research and benefit our technological advancement. It has, however, shown to be difficult to understand and develop models of reactions from fundamental *ab initio* theory [1].

The way we gather data on nuclei today is through scattering experiments, mostly by measuring cross sections [2] since we mainly study radioactive nuclei through beams in accelerators. To calculate these cross sections, one needs an effective potential, modelling the interaction. These are the optical model potentials.

Optical models can be divided into phenomenological, in which a potential is found by fitting experimental data to a model, and microscopic, in which the potential is extracted from detailed calculations of nuclear structure and reactions. Some examples of the phenomenological ones are the parametrization by A.J. Koning and J.P. Delaroche [3] and the potential by F. Perey and B. Buck [4] and a microscopic model is that outlined by A. Idini [5]. In this thesis we will try to bridge the gap between the microscopic optical potentials and the phenomenological ones.

In the following I will introduce nuclear reactions in section 1.1, describe the concept of optical potentials and present some examples of them in section 2 and perform volume integrals and projection between the potentials to analyse the shape of the microscopic model potential in section 3.

1.1 Introductions to nuclear reactions

If a nucleus (A) is incident on another nucleus (B) and the result of the collision might be different nuclei or particles C and D, we write the reaction as $A + B \rightarrow C + D$. In such a reaction, we refer to $A + B$ as the entrance channel and $C + D$ as the exit channel. It is common to denote this reaction as $B(A, C)D$. (Cf. Chapter 2 of [6]).

Reactions usually start of with A and B in their ground states. If they remain in this state, we refer to the reaction as elastic scattering, which we write as B(A,A)B. The traveling direction of the nuclei will have changed at a scattering angle θ after such a reaction, but their relative kinetic energies will remain unchanged. If at least one of the nuclei become

excited, the reaction is referred to as inelastic scattering and the excited state is denoted by a *, meaning that the reaction will therefore be written as $B(A, A)B^*$ if B ends up in the excited state. The kinetic energy of the system will have decreased by the amount ϵ_b of energy that has gone into exciting the nucleus.

If instead a nucleus deposits a neutron onto a target, the reaction is called a neutron transfer reaction. Such a reaction would look like $(A = C + n) + B \rightarrow C + (D = B + n)$, where the nucleus A consists of a core C and a neutron n. This nucleus undergoes a transfer reaction with B, which results in C and D, where D now has B as a core with an extra neutron, n. The final nucleus may be in excited states. We also have the reactions involving photon emission or absorption, $A + B \rightarrow C + \gamma$ and $C + \gamma \rightarrow A + B$, denoted as photodisintegration or radiative capture respectively.

The wave function ψ of a reaction between a projectile and a target nucleus consists of an entrance channel in the form of a plane wave and an exit channel in the form of spherical waves. In order to describe the system before and after scattering, we denote the entrance channel with index α and the different exit channels of the kind described above, with the index β. The quantum mechanical wave function is described as the linear combination of all entrance and exit channels,

$$\psi = \phi_\alpha(\xi_\alpha)e^{i\vec{K}_\alpha\cdot\vec{r}_\alpha} + \sum_\beta \phi_\beta(\xi_\beta)f_\beta(\theta)\frac{e^{i\vec{K}_\beta\cdot\vec{r}_\beta}}{r_\beta}, \tag{1}$$

where $\phi(\xi)$ is the wave function of the nucleus internal degrees of freedom, ξ and r refers to the internal and relative coordinates respectively. $f_\beta(\theta)$ is the scattering amplitude, describing how much the projectile scatters at a given scattering angle θ and $\vec{K}$ is the wave vector [7]. The scattering angle is the angle that separates the travelling direction of the exit channel and the entrance channel. This wave function is a combination of the incoming wave, $\phi_\alpha(\xi_\alpha)e^{i\vec{K}_\alpha\cdot\vec{r}_\alpha}$, that has the form of a plane wave and the sum of all exit channels, $\sum_\beta \phi_\beta(\xi_\beta)f(\theta)\frac{e^{i\vec{K}_\beta\cdot\vec{r}_\beta}}{r_\beta}$, which have the forms of spherical waves. It is determined by solving the Schrödinger equation.

The Schrödinger equation describing the exit channel with a solution of the form described in Eq. (1) is

$$\left[-\frac{\hbar^2}{2\mu_\beta}\nabla_\beta^2 + H_\beta(\xi_\beta) + V_\beta(r_\beta, \xi_\beta) - E\right]\psi^{(+)}(r_\beta, \xi_\beta) = 0 \tag{2}$$

where the first term is the kinetic energy, T, the second term is the internal Hamiltonian, the third term is the potential describing the interaction between projectile and target

and E is the energy of the projectile (cf. Hagino et al. [8]). The Schrödinger equation is often considered an eigenvalue problem, but this is not the case here. Given an incident wave function at a given energy and a given interaction potential, we are looking for the scattered wave and not the steady states represented by eigenstates of the Hamiltonian. Solving it as an eigenvalue problem would give us discrete energy eigenvalues, while we have a continuos range of energies that the particles could be incident with. In other words, we have particles propagating freely except for during the collision and solving it as an eigenvalue problem would introduce boundary conditions we do not have. We assume that the eigenfunctions and eigenvalues of the internal Hamiltonian are known as

$$H_\beta(\xi_\beta)\phi_n = \epsilon_n \phi_n. \tag{3}$$

Considering that the internal and relative degrees of freedom are factorized, note that, $H_\beta \psi^{(+)} = \epsilon_\beta \psi^{(+)}$. Introducing a solvable auxiliary potential, $U_\beta(r_\beta)$, the Schrödinger equation becomes treatable perturbatively. We rewrite the equation as

$$\left(-\frac{\hbar^2}{2\mu_\beta}\nabla_\beta^2 - (E-\epsilon_\beta) + U_\beta\right)\psi^{(+)} + (V_\beta - U_\beta)\psi^{(+)} = 0. \tag{4}$$

We recognize that $E - \epsilon_\beta = \frac{\hbar^2 K_\beta^2}{2\mu_\beta}$, simplifying the equation into

$$\left[-\nabla_\beta^2 - K_\beta^2 + \frac{2\mu_\beta}{\hbar^2}U_\beta(r_\beta)\right]\psi^{(+)} = -\frac{2\mu_\beta}{\hbar^2}(V_\beta - U_\beta)\psi^{(+)}. \tag{5}$$

The left hand side is now the Hamiltonian for elastic scattering and the right hand side can be considered a perturbation to this Hamiltonian. The Schrödinger equation describing any exit channel can therefore be thought of as a perturbation of an elastic scattering process over an auxiliary potential. This auxiliary potential is called the optical model potential which is therefore an essential topic of research in nuclear physics since it describes the elastic scattering in nuclear reactions.

2 Methods: Optical potentials

The optical potential has been used to analyse elastic scattering of particles over a wide range of energies for several decades. It represents the auxiliary potential modelling the reaction in the elastic channel and it is therefore used to calculate other direct reactions. Historically it is constructed by a phenomenological potential of a relatively simple form

fitted to elastic scattering data. It is a complex potential, with the imaginary part dealing with the possibility of the wave function being absorbed by the target, resulting in other possible channels of interaction, e.g. non-elastic scattering. The optical potential is generally written in the form

$$U = (V + iW)f(r), \tag{6}$$

where U and W are the potential depths for the real and imaginary parts respectively. The form factor $f(r)$ is typically given as a Woods-Saxon (WS) form,

$$f(r) = \frac{1}{1 + \exp\left(\frac{r-R_i}{a_i}\right)}, \tag{7}$$

where R_i is the radius found by $R_i = r_i A^{1/3}$, for a given nuclear mass A, and a_i is the surface diffuseness parameter, with r_i and a_i parameters measured in fm. This form is a good representation of the average potential related to the nuclear density, which is necessary for an accurate model of nuclear scattering. In some models, a better agreement with experiment is achieved by allowing these parameters in the form factor to differ between the real and imaginary potentials.

At low energies the projectile does not penetrate deep into the target and the reaction mainly takes place at the surface of the nucleus. Therefore, some analyses use a form factor that peaks at the surface of the target for the imaginary depth. This surface-peaked form factor has the shape

$$g(r) = -4a_i \frac{d}{dr} f(r). \tag{8}$$

The reason for the factor $-4a_i$ is to make sure that $g(R) = 1$. In order for the polarisation of the scattered particle to be able to be calculated, the spin-orbit coupling has to be taken into account. This is done with a spin-orbit term in the potential,

$$V_{SO}(r) = (U_s + iW_s)\left(\frac{\hbar}{m_\pi c}\right)^2 \frac{1}{r}\frac{d}{dr} f(r), \tag{9}$$

where U_s is the real depth and W_s is the imaginary depth. The latter is often not included since this additional parameter has not shown to improve agreement with the data [9].

This results in a nine parameter potential if the imaginary spin-orbit potential is excluded or an eleven parameter one if it is included. One well known parametrization of the eleven parameter potential was developed and presented by A.J. Koning and J.P. Delaroche in 2001 [3].

2.1 Koning-Delaroche Potential

A.J. Koning and J.P. Delaroche created a global optical model parametrization for neutrons and protons to predict basic scattering observables over a range of energy and nuclei. This would make it no longer necessary to use different optical models in different energy ranges. One of the assumptions made was to model the nuclides with near-spherical potential distributions.

The optical potential that was parametrised in [3] looks like

$$\mathcal{U}_{KD}(r,E) = -\mathcal{V}_V(r,E) - i\mathcal{W}_V(r,E) - i\mathcal{W}_D(r,E) + V_{SO}(r,E) + i\mathcal{W}_{SO}(r,E) + \mathcal{V}_C(r), \quad (10)$$

where each term represents the different contributions to the potential. All of the components are separated in different well depths, with their respective form factors,

$$\mathcal{V}_V(r,E) = V_V(E)f(r), \quad (11)$$

$$\mathcal{W}_V(r,E) = W_V(E)f(r), \quad (12)$$

$$\mathcal{W}_D(r,E) = W_D(E)g(r), \quad (13)$$

$$\mathcal{V}_{SO}(r,E) = V_{SO}(E)\left(\frac{\hbar}{m_\pi c}\right)^2 \frac{1}{r}\frac{d}{dr}f(r), \quad (14)$$

$$\mathcal{W}_{SO}(r,E) = W_{SO}(E)\left(\frac{\hbar}{m_\pi c}\right)^2 \frac{1}{r}\frac{d}{dr}f(r). \quad (15)$$

This model describes the potential depths, V_i, W_i, using a unique energy dependent form which is one of the most used optical models to date [3, 10]. The depths of the parts with the WS form factor, referred to as the volume-central potential, indexed with V, are determined by

$$V_V(E) = v_1\left(1 - v_2(E-E_f) + v_3(E-E_f)^2 - v_4(E-E_f)^3\right), \quad (16)$$

for the real part and

$$W_V(E) = w_1\frac{((E-E_f)^2)}{(E-E_f)^2 + w_2^2}, \quad (17)$$

for the imaginary part. The depth of the part with the surface-peaked form factor, referred to as the surface-central potential, indexed with D, are found using

$$W_D(E) = d_1\frac{((E-E_f)^2)}{(E-E_f)^2 + d_3^2}\exp(-d_2(E-E_f)) \quad (18)$$

and for the spin-orbit part we have the real depth as

$$V_{SO} = v_{SO1}\exp(-v_{SO2}(E-E_f)) \quad (19)$$

and the imaginary depth as

$$W_{SO} = w_{SO1} \frac{((E - E_f)^2)}{(E - E_f)^2 + w_{SO2}^2}. \tag{20}$$

In this work we will consider only neutron scattering and will therefore neglect the Coulumb term, V_C. The parameters v_i, w_i and d_i for the different parts are real numbers and were found through extensive grid search and a computational steering technique, as tabulated in [10]. E is the energy of the projectile and E_f is the Fermi energy [3]. The Koning-Delaroche (KD) potential thus becomes a function of both the relative distance and kinetic energy of the reaction. Furthermore, it becomes dependant on the target and whether the projectile is a neutron or a proton.

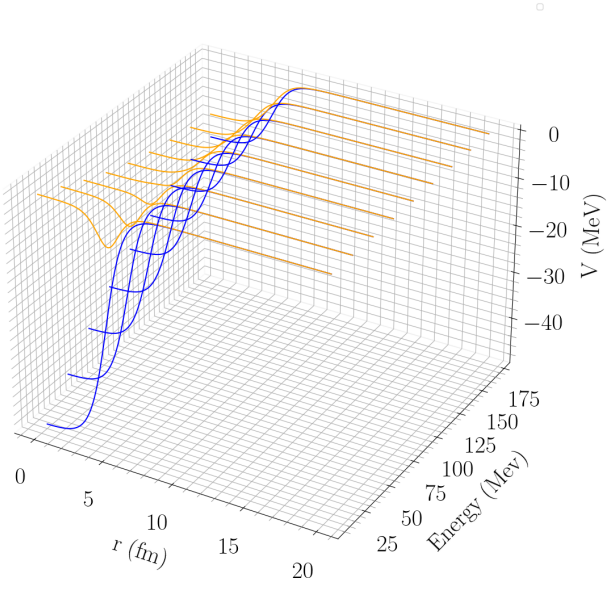

Figure 1: The potential depth of the real part (blue) and the imaginary part (orange) of the Koning-Delaroche potential. The potential is illustrated at radial distances up to 20 fm with incident energies between 0 and 200 MeV for a neutron scattering of ^{56}Fe.

In Fig 1 we see the real and imaginary part of the KD potential for a neutron incident on ^{56}Fe at energies ranging from 0 to 200 MeV. At lower energies we see that the imaginary part takes a surface-peaked form, since the projectile should not penetrate beneath the surface. At higher energies the imaginary potential becomes deeper further in into the target as expected.

2.2 Perey-Buck potential

F. Perey and B. Buck investigated the possibility of representing the energy dependence of the phenomenological local potentials using only a non-locality, i.e. a dependence on two coordinates [4]. To aid in numerical calculations, the form of the potential was chosen to be separable and looks like

$$V(r,r') = U\left(\frac{1}{2}(r+r')\right) H(r-r'). \tag{21}$$

The operator acts like

$$V\psi(r) = \int V(r,r')\psi(r')dr'. \tag{22}$$

The factors of the potential were chosen to be a Gaussian function

$$H(r-r') = \frac{1}{\pi^{\frac{3}{2}}\beta^3} e^{-\frac{(r-r')^2}{\beta^2}} \tag{23}$$

and a form similar to the KD potential,

$$-U(\tilde{r}) = V_R f_R(\tilde{r}) + iW_I f_I(\tilde{r}) + iW_D f_D(\tilde{r}). \tag{24}$$

Here $\tilde{r}$ has been defined as $\tilde{r} = \frac{1}{2}(r+r')$. The form factors were defined as the WS,

$$f_V(\tilde{r}) = \left[1 + \exp\left(\frac{\tilde{r} - R_V}{a_V}\right)\right]^{-1}, \tag{25}$$

and its derivative,

$$f_D(\tilde{r}) = 4\exp\left(\frac{\tilde{r} - R_D}{a_D}\right)\left[1 + \exp\left(\frac{\tilde{r} - R_D}{a_D}\right)\right]^{-2}, \tag{26}$$

similarly to the KD potential. The parameters of the potential were originally fitted to scattering data for neutron scattering of ^{56}Fe and used for the non-local potential at other energies. The parameters used are presented in Table 1 and were taken from a modern parametrization and fitting of the potential [11].

Table 1: The parameters used in the PB potential.

V_R	r_R	a_R	W_I	r_I	a_I
70.00	1.25	0.61	1.39	1.17	0.55
W_D	r_D	a_D	β		
21.11	1.15	0.46	0.90		

In Fig 2 we see the real part (blue) and imaginary part (red) of the PB potential as described above for radial distances up to 10 fm. Note that the general shape of the potential, at least in the diagonal, is similar to that of the KD potential, with the surface peak in the imaginary part and the potential vanishes as the nuclei are separated.

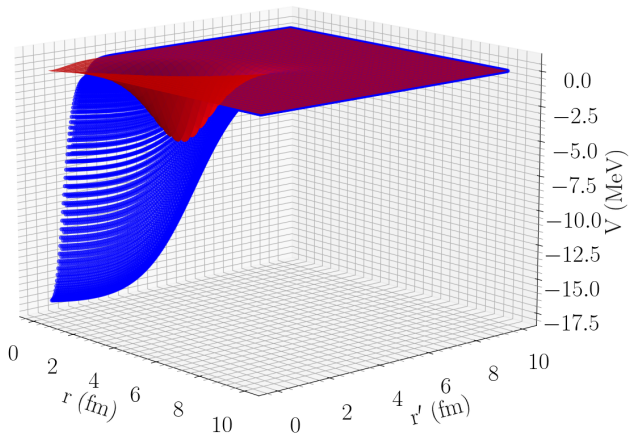

Figure 2: The potential depth of the real part (blue) and the imaginary part (orange) of the Perey-Buck potential. The potential is illustrated at radial distances up to 10 fm with parameters as seen in Table 1.

2.3 Microscopic optical potentials

The main idea of the microscopic optical model is to extract an effective potential from calculations of interacting nucleons composing the nuclei. The non-phenomenological microscopic approach is used since the optical model separates the projectiles scattering wave function from the targets internal structure. One of the possible approaches is the self-consistent Green's function formalism that was used in [5].

The benefit of the microscopic model is the fact that it does not require previous data on the nuclei it is made to model. Since it is based on microscopic calculations, it is more applicable to nuclei not yet discovered and those where the phenomenological fit is unreliable [12].

In the microscopic model, the optical potential is expressed in an orbital basis of principal

quantum number, n. The interaction between two nucleons in two orbital states is represented as $V^{l,j}_{n,n'}$ for a given orbital angular momentum, l, and total angular momentum, j. Therefore, in coordinate space, it is expressed as

$$V^{l,j}(r,r') = \sum_{n,n'} R_{n,l}(r) V^{l,j}_{n,n'} R_{n',l}(r'), \tag{27}$$

where $R_{n,l}(r)$ are orbital wavefunctions, such as the radial harmonic oscillator wave functions. This describes the communication between two orbitals and is non local [5].

Another example of an *ab initio* nucleon nucleus optical potential can be made by combining the Green's function approach with the symmetry-adapted no-core shell model (SA-NCSM). In an orthonormal basis, the Green's functions that characterizes the interactions are calculated, using relevant fundamental operators such as the particle number operator and the Hamiltonian. The effective potential in this model can be extracted using the inverse of the Green's function. The potential is expressed using single-particle wavefunctions in configuration representation within a harmonic oscillator basis [13].

The microscopic approach used for comparison here is derived from self-consistent Green's function theory (SCGF) as outlined by A. Idini et al. [5] for ^{16}O.

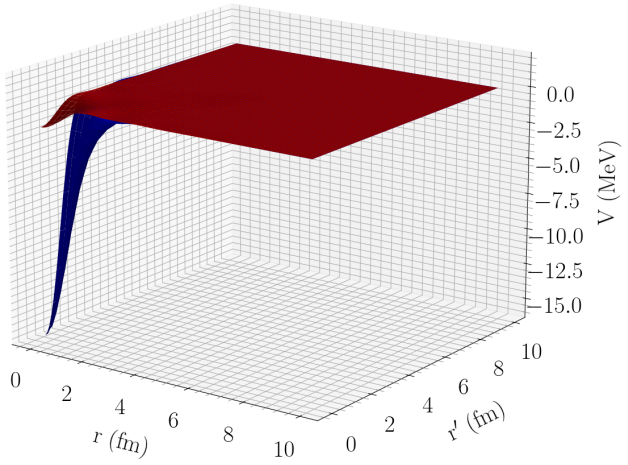

Figure 3: The potential derived from self consistent Green's function theory for ^{16}O, with l=0 and j=1/2, for an incident energy of 10 MeV. The real part is depicted in blue and the imaginary in red.

In Fig 3 we see the SCGF potential from [5] for a neutron incident on ^{16}O with an energy of 10 MeV and l=0 and j=1/2. The real part (blue) has a deeper depth than the imaginary part (red) and both parts are deeper at closer distances to the centre of the nucleus. It can also be seen that the potential is deeper along the r = r′ diagonal. This line will be referred to as the main valley. The surface peak seen in the KD and PB potentials is not clearly visible here but the general shape of the potential is otherwise the same.

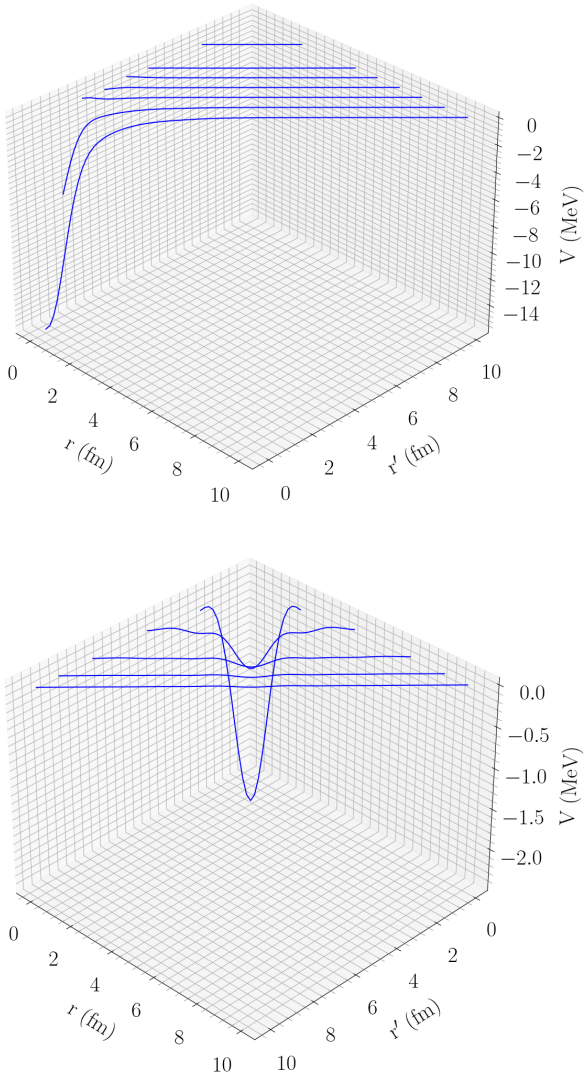

Figure 4: Segments of the real part of the SCGF potential, for a neutron incident on ^{16}O with energy 10 MeV, l=0 and j=1/2, at some distances from the target taken parallel to the main valley $V_{SCGF}(r, r' = r + \delta)$ (top) and perpendicular to it $V_{SCGF}(r, r' = \delta - r)$ (bottom) for a few values of δ.

In Fig 4 we see some segments, $V_{SCGF}(r, r' = r+\delta)$ (top) and $V_{SCGF}(r, r' = \delta - r)$ (bottom), of the real part of the same potential as in Fig 3. We see that the depth becomes deeper further into the target and the potential vanishes at greater distances.

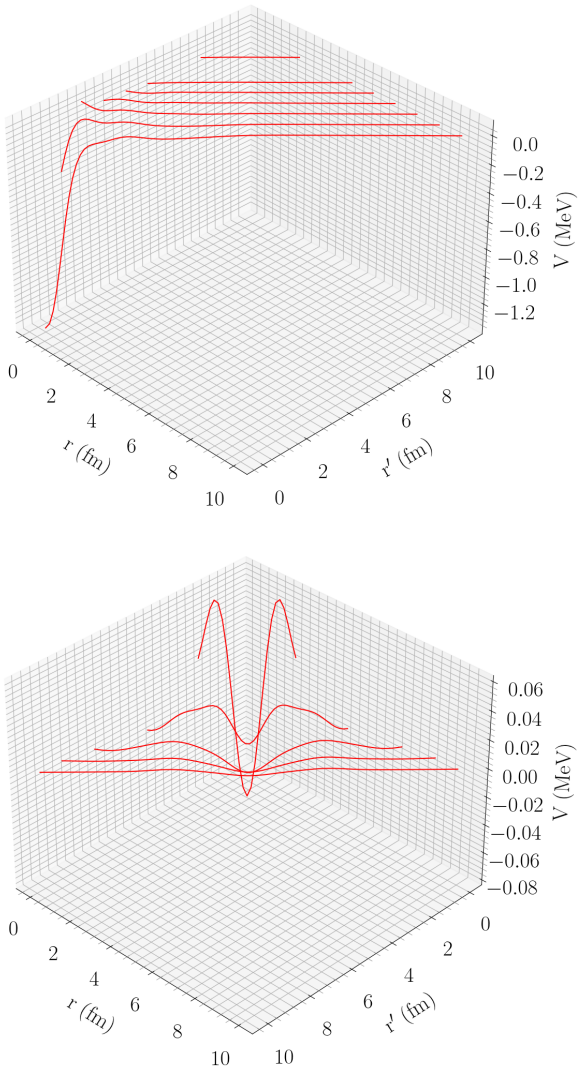

Figure 5: Segments of the imaginary part of the SCGF potential, for a neutron incident on ^{16}O with energy 10 MeV, l=0 and j=1/2, at some distances from the target taken parallel to the main valley $V_{SCGF}(r, r' = r + \delta)$ (top) and perpendicular to it $V_{SCGF}(r, r' = \delta - r)$ (bottom) for a few values of δ.

In Fig 5 we see some segments, $V_{SCGF}(r, r' = r + \delta)$ (top) and $V_{SCGF}(r, r' = \delta - r)$ (bottom), of the imaginary part of the same potential as in Fig. 3. We see that the potential depth increases further into the target and vanishes outside of it. We also notice

that the potential increases, even becomes positive, just outside of the main valley. Here, and in Fig. 4, we have a better depiction of the main valley of the imaginary part of the potential.

3 Results

3.1 Volume Integral

By calculating the volume integral of the real part, J_V, and the imaginary part, J_W, of the KD potential 10,

$$J_V = \int \Re\left(V(r)\right) dV \tag{28}$$

$$J_W = \int \Im\left(V(r)\right) dV, \tag{29}$$

it can be compared to a potential derived from non-phenomenological analyses, such as microscopic approaches. In Fig 6 and 7 the volume integral per nucleon is presented for the real and imaginary part of the KD potential respectively. It has been calculated for incident neutrons with energies of 1, 10 and 200 MeV. For simplicity, the nucleus has been modelled to have a total of A nucleons and A/2 protons. These integrals follow the same trend as presented in the original paper [10].

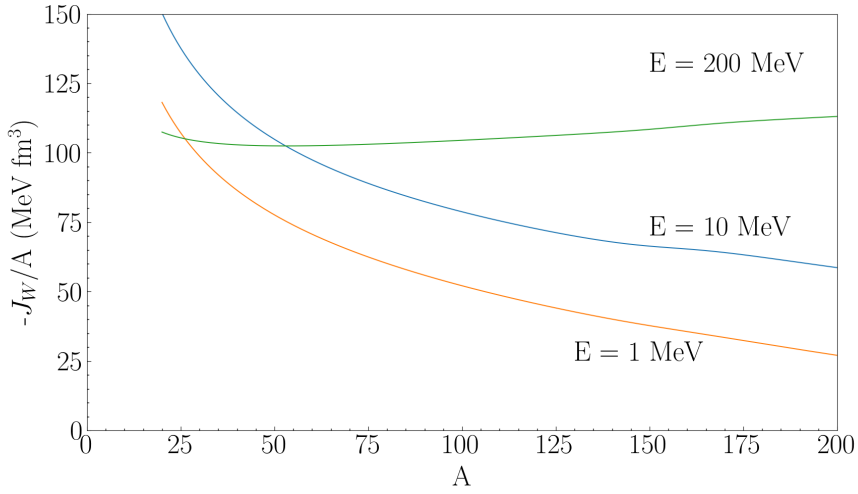

Figure 6: Volume integral per nucleus J_W/A for an incident neutron on the imaginary part of the KD potential as a function of nuclear mass, A, for 1, 10 and 200 MeV energy, assuming $N = Z = A/2$.

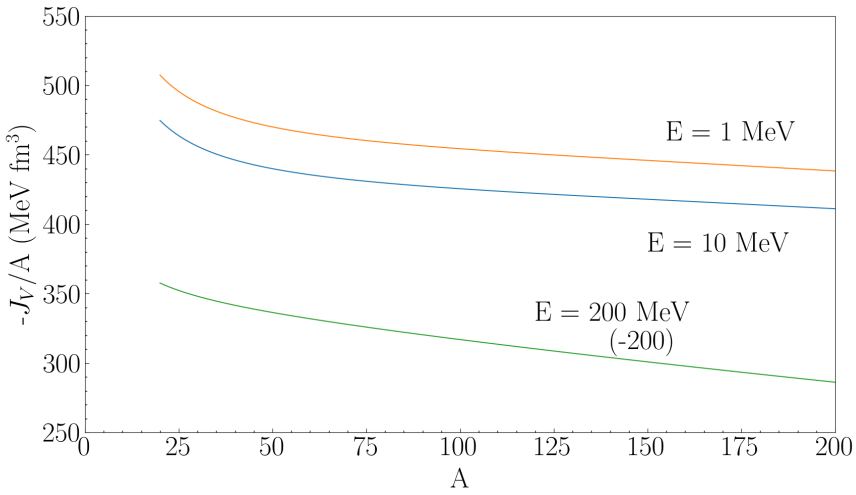

Figure 7: Volume integral per nucleus J_W/A for an incident neutron on the real part of the KD potential as a function of nuclear mass, A, for 1, 10 and 200 MeV energy, assuming $N = Z = A/2$. For illustrative purposes, the volume integral at 200 MeV has been increased by 200 MeV fm^3.

We now start comparing the volume integrals of the two potentials. In Fig 8 and 9 we see the volume integral per nucleon for the imaginary and real part of the potential from SCGF (orange) and for the KD potential (blue) respectively for a neutron incident on ^{16}O with l=0 and j=1/2.

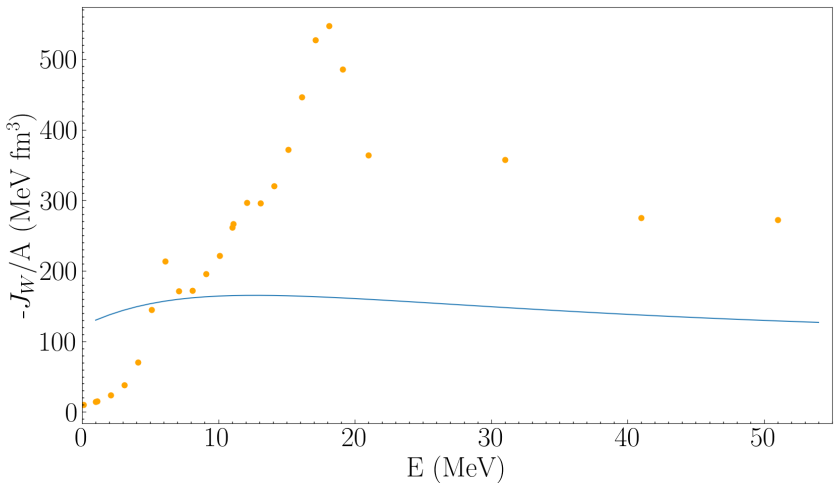

Figure 8: The volume integral per nucleus of the imaginary part of the potential for a neutron incident on ^{16}O as a function of energy. The SCGF potential for $l = 0$ and $j = 1/2$ in orange and the KD potential in blue.

For the imaginary part, we see that the two models seem to agree at some energies but as the energy of the projectile increases, they start to differ more. They seem to be in agreement mostly around 10 MeV, but even elsewhere they are within about a factor of two from each other.

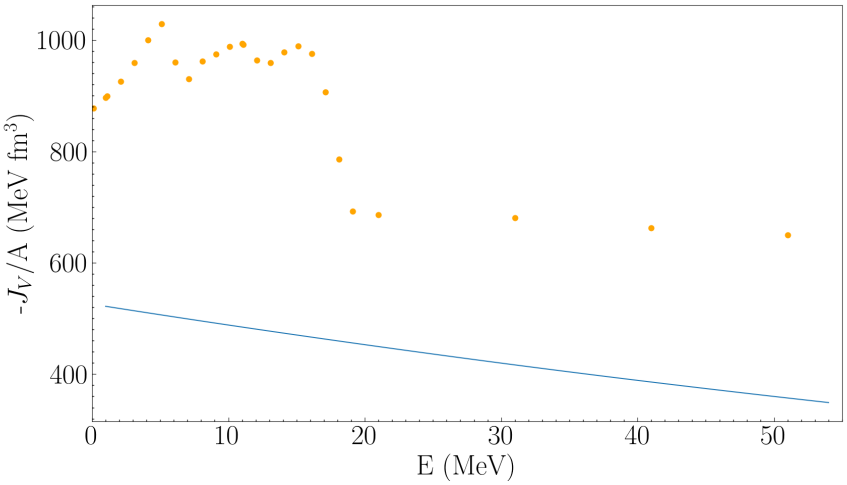

Figure 9: The volume integral per nucleus of the real part of the potential for a neutron incident on ^{16}O as a function of energy. The SCGF potential for $l = 0$ and $j = 1/2$ in orange and the KD potential in blue.

The real part of these potentials seem to be in less agreement, but the general trend of the volume integral is somewhat similar. In both cases the volume integral flattens out at higher energies. We also see that there is only about a factor of two difference between the volume integrals of the potentials The SCGF potential seems to have a larger volume integral in general but we have yet to compare the shapes of the potentials, that is the most important part.

3.2 Projection

We now compare the potentials. We can consider the potentials as elements of the L^2 Hilbert space. The norm in this space is defined as

$$||f(x)|| = \sqrt{\int \|f(x)\|^2 \, dx}, \tag{30}$$

for a function $f(x) \in L^2$. The inner product between two functions in this space, f and g, is defined as

$$f \cdot g = \int f(x)g(x)dx. \tag{31}$$

We want to find the projection, α, of one function, f, onto the another, g. In terms of the inner product and norm, it is

$$\alpha = \frac{f \cdot g}{||f|| \cdot ||g||}. \tag{32}$$

However, since the SCGF potential is dependent on two variables, r and r$'$, while the KD potential depends only on r, the potentials belong to different vector spaces and this projection is not well defined. There are a few different approaches to move these potentials into the same vector space. One of them is to consider segments of the SCGF potential such that Eq. (32) becomes

$$\alpha_{KD}^{SCGF}(r'') = \frac{V_{SCGF}(r, r' = r + r'') \cdot V_{KD}(r)}{||V_{SCGF}|| \cdot ||V_{KD}||} \tag{33}$$

Now we have a projection onto a diagonal parallel to the main valley of the SCGF potential with an offset of r$''$. We can then calculate the projections onto these diagonals.

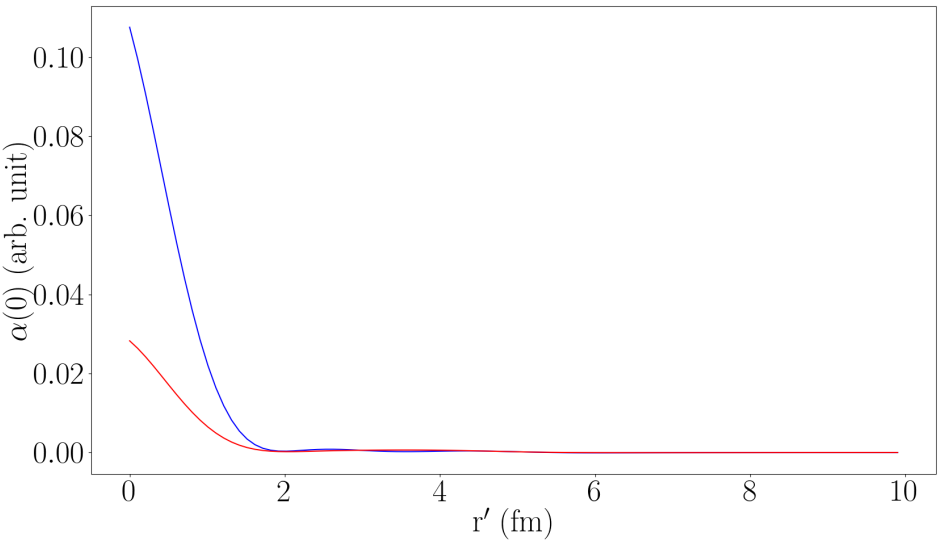

Figure 10: Diagonals parallel to the main valley of the SCGF potential for a neutron incident on ^{16}O with energy 10 MeV, l=0 and j=1/2, offset with r″ as $V_{SCGF}(r, r + r')$, projected onto the KD potential for a neutron incident on ^{16}O with an energy of 10 MeV. The real part is depicted in blue and the imaginary part in red.

In Fig 10 we see the projections as described by Eq. (33) as a function of r′ for a neutron incident on ^{16}O with an energy of 10 MeV. We see that the real parts overlap more than the imaginary parts and it seems to be greater for smaller r″. The reason for the zero values further out from the nucleus is not that they overlap less. The reason is that the values of the potentials here are zero, so the projection becomes zero.

Another approach to the projection is to expand the KD potential into the same vector space as the SCGF potential. This is done by redefining the potential as

$$V_{KD}(r) \to V_{KD}\left(\frac{1}{2}(r + r')\right) g(r - r'), \tag{34}$$

where $g(r - r')$ is a Gaussian. This means that we can rewrite Eq. (32) as

$$\beta = \frac{V_{KD}\left(\frac{1}{2}(r + r')\right) g(r - r') \cdot V_{SCGF}(r, r')}{||V_{SCGF}|| \cdot ||gV_{KD}||}. \tag{35}$$

We note that the product $V_{KD}\left(\frac{1}{2}(r + r')\right) g(r - r')$ is quite similar to the PB potential and we will therefore directly analyse this instead. This projection now become

$$\beta = \frac{V_{PB}(r, r') \cdot V_{SCGF}(r, r')}{||V_{SCGF}|| \cdot ||V_{PB}||}. \tag{36}$$

At this point, since both potentials depends on both r and r′, they are in the same vector space and we define the projection of $f, g \in L^2$ onto each other as

$$\beta = \frac{f(r,r') \cdot g(r,r')}{||f|| \cdot ||g||} = \frac{1}{||f|| \cdot ||g||} \int g(r,r') f(r,r') dr dr'. \tag{37}$$

We evaluate the projection of the SCGF potential for l = 0, j = 1/2 and an incident energy of 10 MeV, onto the PB potential and find it to be about $\beta_{PB}^{SCGF} = 0.765$ for the real part and $\beta_{PB}^{SCGF} = 0.821$ for the imaginary part. That means that the shapes of the PB and SCGF potentials real parts overlap with 76.5% and the imaginary parts overlap with 82.1%.

The value derived for the projection of the SCGF potential onto the PB potential used an incident energy of 10 MeV. For energies other than this, the projection should change. The PB potential is not dependent on the energy, but the SCGF potential is. By calculating the same projection for a range of incident energies we can compare the potentials further.

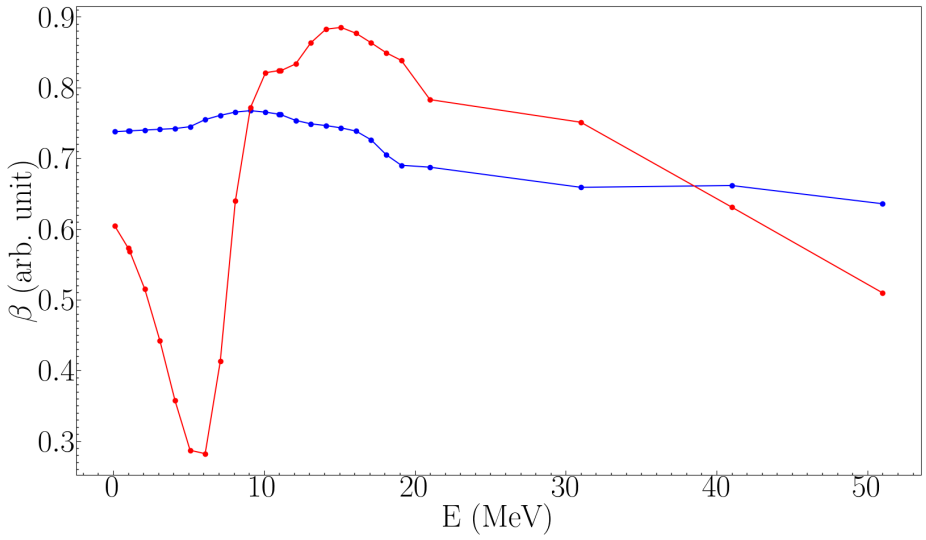

Figure 11: The real (blue) and imaginary (red) part of the projection of the SCGF potential for a neutron incident on ^{16}O with l=0 and j=1/2, on the PB potential for different energies. Solid lines are included to guide the eye.

In Fig 11 we see the projection of the SCGF potential for a neutron incident on ^{16}O with l=0 and j=1/2, on the PB potential for energies ranging from 0 to 50 MeV. It can be seen

that the two models are in agreement at energies between 10 and 20 MeV as opposed energies outside of this range, where they do not overlap as much.

So far we have considered the case where there is no angular momentum, i.e. $l = 0$. If we want to compare how the models change as the angular momentum increases, we need to add the centrifugal term

$$\tilde{V} = V + \frac{l(l+1)}{r^2 2\mu}, \tag{38}$$

where μ is the reduced mass. This is simply added to the KD potential to take the angular momentum into account. We can now project the main valley of the SCGF potential, $V_{SCGF}(r, r' = r)$ onto the KD potential, with the centrifugal term included, $\tilde{V}_{KD}$, for every l.

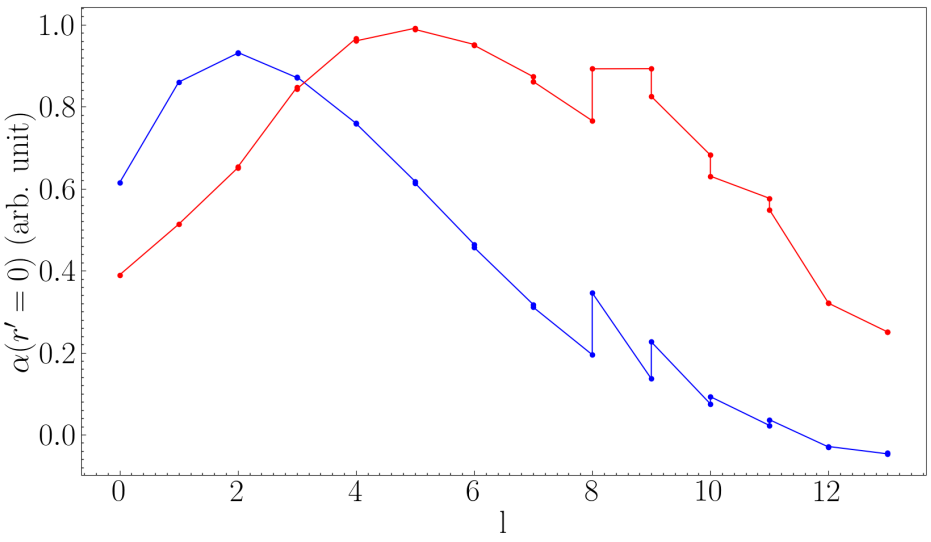

Figure 12: The projection of the main valley of the SCGF potential, $V_{SCGF}(r, r' = r)$ onto the KD potential for different l. The real part in blue and the imaginary part in red. The potentials represent a neutron incident on ^{16}O with an energy of 10 MeV. The two values seen for the projection at each l, is caused by the value for j being $j = l \pm \frac{1}{2}$. Solid lines to guide the eye.

In Fig 12 we see the behaviour of the projection of the SCGF onto the KD potential including the centrifugal term for a neutron incident on ^{16}O with an energy of 10 MeV. The projection has two values for each l since the value for j is $j = l \pm \frac{1}{2}$. The projection seem to be worse at higher angular momenta and much better at the lower ones. From

here on out, we will only consider the $l = 0$ momentum.

3.3 Projection onto analytical form

We now want to project the SCGF potential onto an analytical expansion which could form a basis for the L^2 Hilbert space. The form we are using is the general form of an optical potential

$$U(r, r') = V(r, r') + iW(r, r'), \tag{39}$$

The potential depths will be represented in the expansion by the Gaussian and the WS and their corresponding derivatives. We use this expansion since it is known that the derivative of a function in L^2 has an orthogonal component to the function itself. It should therefore be possible to form a basis from these. The real potential is defined as

$$\begin{aligned} V(r, r') =& \alpha_{11} f_1(\frac{r + r'}{2}, R_{11}, a_{11}) g_1(r - r', c_{11}) && (40)\\ &+ \alpha_{12} f_1(\frac{r + r'}{2}, R_{12}, a_{12}) g_2(r - r', c_{12}) && (41)\\ &+ \alpha_{13} f_2(\frac{r + r'}{2}, R_{13}, a_{13}) g_1(r - r', c_{13}) && (42)\\ &+ \alpha_{14} f_2(\frac{r + r'}{2}, R_{14}, a_{14}) g_2(r - r', c_{14}) && (43) \end{aligned}$$

and the imaginary, where we allow for more complex behaviour, as

$$\begin{aligned} W(r, r') =& \alpha_{21} f_1(\frac{r + r'}{2}, R_{21}, a_{21}) g_1(r - r', c_{21}) && (44)\\ &+ \alpha_{22} f_1(\frac{r + r'}{2}, R_{22}, a_{22}) g_2(r - r', c_{22}) && (45)\\ &+ \alpha_{23} f_1(\frac{r + r'}{2}, R_{23}, a_{23}) g_3(r - r', c_{23}) && (46)\\ &+ \alpha_{24} f_2(\frac{r + r'}{2}, R_{24}, a_{24}) g_1(r - r', c_{24}) && (47)\\ &+ \alpha_{25} f_2(\frac{r + r'}{2}, R_{25}, a_{25}) g_2(r - r', c_{25}) && (48)\\ &+ \alpha_{26} f_2(\frac{r + r'}{2}, R_{26}, a_{26}) g_3(r - r', c_{26}). && (49) \end{aligned}$$

The form factors choosen here are the WS

$$f_1(p, R, a) = \frac{1}{(1 + \mathrm{e}^{\frac{r-R}{a}})} \tag{50}$$

$$f_2(p, R, a) = f_1'(p, R, a) - (f_1'(p, R, a) \cdot f_1(p, R, a))\, f_1(p, R, a) \tag{51}$$

and the Gaussian

$$g_1(q,c) = e^{\frac{-x^2}{2c^2}} \tag{52}$$

$$g_2(q,c) = \frac{d^2}{dq^2}g_1(q,c) - \left(\frac{d^2}{dq^2}g_1(q,c)\cdot g_1(q,c)\right)g_1(q,c) \tag{53}$$

$$g_3(q,c) = \frac{d^4}{dq^4}g_1(q,c) - \left(\frac{d^4}{dq^4}g_1(q,c)\cdot g_1(q,c)\right)g_1(q,c) - \left(\frac{d^4}{dq^4}g_1(q,c)\cdot g_2(q,c)\right)g_2(q,c) \tag{54}$$

in combination with their derivatives, orthogonalized using the Gram Schmidt method. The parameters are then determined by projecting the SCGF potential onto this analytical form as

$$\alpha_{ik} = \frac{V_{SCGF}\cdot(f_i(\frac{r+r'}{2}, R_{ik}, a_{ik})g_k(r-r', c_{ik}))}{||V_{SCGF}||\cdot||f_i g_k||} \tag{55}$$

and optimizing the projection for each term ik in Eq. (40-49). The optimization is done numerically using the Nelder-Mead method. This is done both for the real and the imaginary parts individually.

In Table 2 we see the parameters found for the real part of the analytical potential for the given index of each term, optimized for a neutron incident on ^{16}O with an energy of 10 MeV.

Index	11	12	13	14
α	-0.270	0.414	0.074	-0.242
R	0.023	0.023	1.725	1.725
a	0.472	0.472	0.689	0.689
c	4.790	1.163	4.790	1.163

Table 2: All parameters for the real part of the analytical potential optimized for the SCGF potential of a neutron incident on ^{16}O with an energy of 10 MeV.

In Table 3 we see the parameters found for the imaginary part of the analytical potential for the given index of each term, optimized for a neutron incident on ^{16}O with an energy of 10 MeV.

Index	21	22	23	24	25	26
α	-0.604	-0.076	-0.079	0.024	-0.172	-0.045
R	4.156	4.156	0.636	0.636	4.156	0.636
a	0.375	0.375	0.561	0.561	0.375	0.561
c	0.826	3.923	0.826	3.923	1.094	1.094

Table 3: All parameters for the imaginary part of the analytical potential optimized for the SCGF potential of a neutron incident on ^{16}O with an energy of 10 MeV.

We now want to investigate how well the analytical potential fits the SCGF potential at other incident energies.

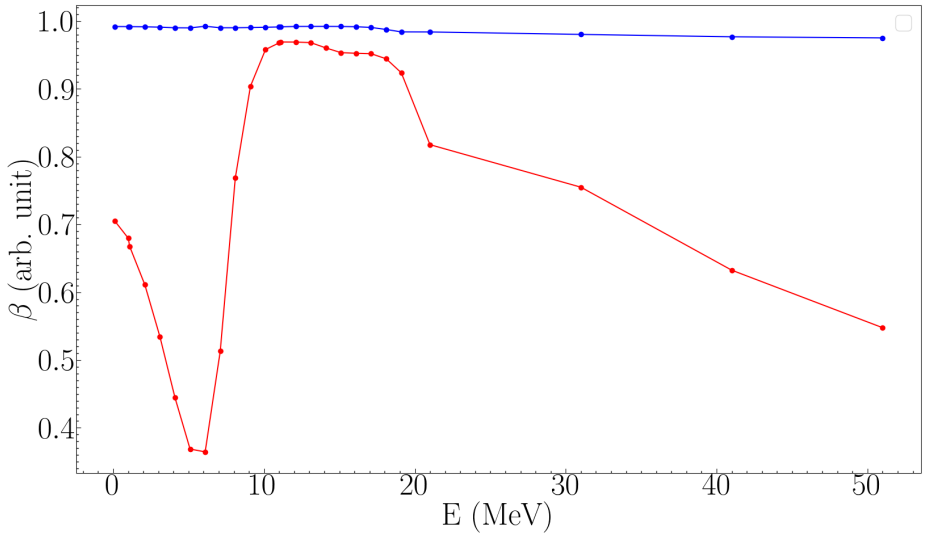

Figure 13: The real (blue) and imaginary (red) part of the SCGF potential projected on the analytical potential (39), optimized for the SCGF potential of a neutron incident on ^{16}O with an energy of 10 MeV, with l=0 and j=1/2, for a range of energies. Solid lines to guide the eye.

In Fig 13 we see the SCGF potential for a neutron incident on ^{16}O with l=0 and j=1/2, projected onto the analytical potential (39) for a range of energies. The analytical potential was optimized for an incident neutron with an energy of 10 MeV. Thus we see that the overlap is greatest at this energy. Similarly to the PB potential in Fig 11 the imaginary part overlaps more at medium energies than at lower or higher ones, in the vicinity of

10 MeV. At even larger energies, the analytical potential becomes a bad approximation. The real part seems to have a fairly constant overlap, but it is greater for the analytical potential than for the PB potential.

We now investigate how the analytical potential changes as it is optimized for different energies. The SCGF potential is projected onto the analytical potential at each energy to see how the projection changes for the different optimizations of the analytical potential.

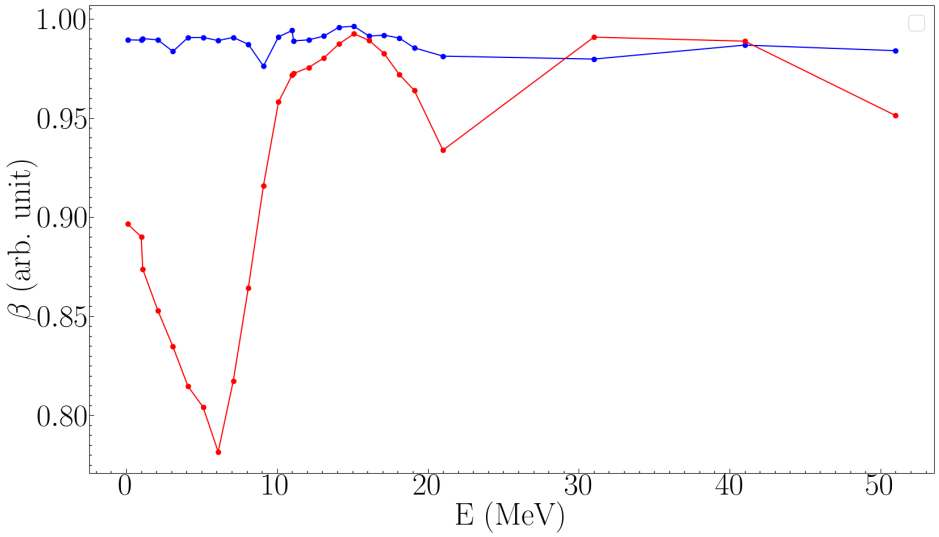

Figure 14: The real (blue) and imaginary (red) part of the SCGF potential projected on the analytical potential (39), optimized for the SCGF potential for a neutron incident on ^{16}O with a range of energies with l=0 and j=1/2. The analytical expansion was optimized for each energy individually. Solid lines are included to guide the eye.

In Fig 14 we see the real (blue) and imaginary (red) part of the projection of the SCGF potential for a neutron incident on ^{16}O with a range of energies with l=0 and j=1/2, projected onto the analytical potential (39). The analytical form was optimized at each energy. The real part is nearly constant but the imaginary part has significantly less overlap at some lower energies than at higher energies.

To get a better insight into the potential, we look at the impact of each term in the analytical representation by determining the magnitude of its contribution to the total potential. We project the SCGF potential onto each term separately.

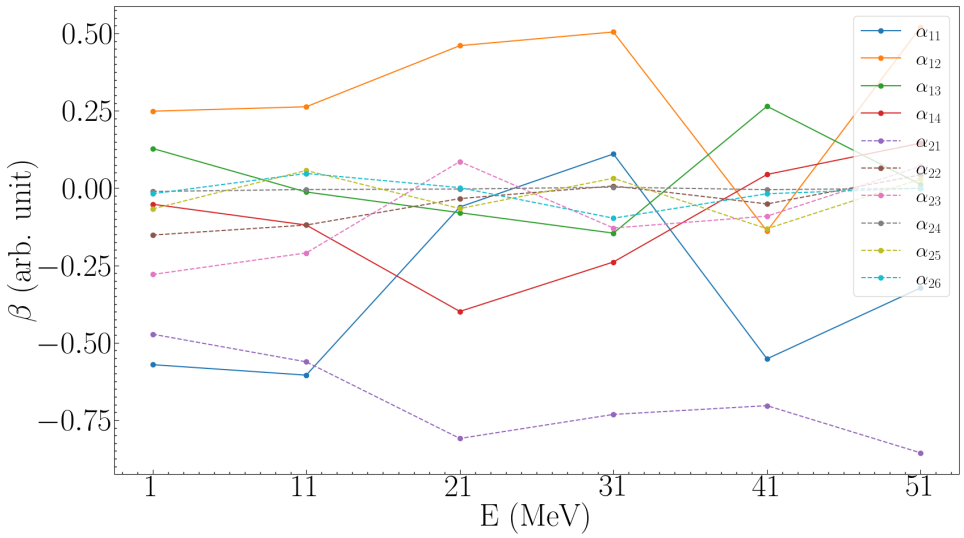

Figure 15: The projection of the SCGF potential for a neutron incident on ^{16}O with l=0 and j=1/2 for a range of energies, onto each term of the analytical potential, α_{ik}, optimized at each incident energy. Solid lines for the real terms and dashed lines for the imaginary terms are included to guide the eye.

In Fig 15 we see the same projection as in Fig 14, but the magnitudes of the different terms are represented instead. The dominating terms are mostly the same for the different energies, with some changes in the subsequently contributing terms. For the real part the dominating term is the one with the WS and the second derivative of the Gaussian as well as the Gaussian itself and for the imaginary part it is the term with the WS and Gaussian. In both cases, the dominating terms accounts for at least half of the magnitude of the potential in total.

To further investigate how each term affects the projection, we add one term at a time to the analytical potential, starting with only the first term. We then project the SCGF potential onto this potential.

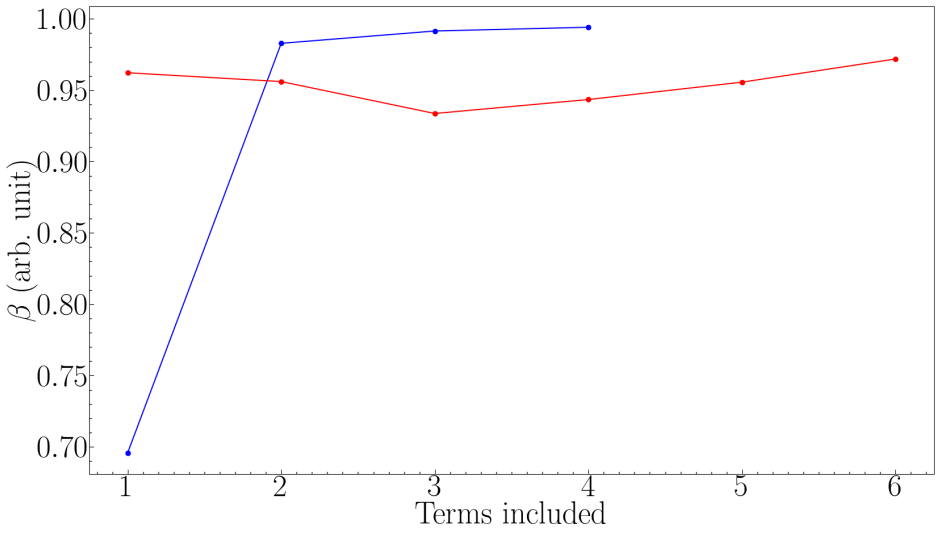

Figure 16: The SCGF potential for a neutron incident on ^{16}O with l=0 and j=1/2, projected onto the analytical potential (39) with an increasing number of terms included for an incident energy of 10 MeV. Solid lines are included to guide the eye.

In Fig 16 we see the SCGF projected onto the analytical potential for a varying number of terms. The real part is depicted in blue and the imaginary part in red. The real part benefits most from the second term, which is the WS multiplied by the second derivative of the Gaussian, further exemplifying the importance of that term. The rest of the terms added to the real part only slightly improves the projection. For the imaginary part we see that the first term, being the WS multiplied by the Gaussian, carries the most importance and the projection becomes fairly high from the start. The rest of the terms only slightly alters the projection.

4 Conclusion

We wanted to bridge the gap between phenomenological and microscopic model potentials by finding a representation of a non-local optical potential for nuclear reactions. This was done through comparative analysis using previously established phenomenological model potentials.

We conclude that the SCGF potential and the KD potential have greatest overlap at angular momenta between $l = 2$ and $l = 5$. At zero angular momentum the overlap is

slightly lower and at higher momentum it falls of. In comparison to the PB potential, the SCGF potential has a similar shape with the greatest projection at energies from 10 to 30 MeV with the best fit at 10 MeV.

The projection onto the analytical potential showed that the real part of the SCGF potential mainly follows the shape of a WS multiplied with the second derivative of the Gaussian as well as the Gaussian itself. Depending on the incident energy, the Gaussian and the derivative of the WS also gives some noticeable improvements to the projection. The imaginary part mainly follows the shape of the WS multiplied by the Gaussian. Some minor improvements in the projection comes from including higher order terms. The impact of the different terms differs based on incident energy and they collectively improve the projection with no specific order of their effect on the projection.

In conclusion, we see that it is possible to represent the microscopic model potential in an analytical form locally with high accuracy, using an approximation of an expansion of a basis for the L^2 Hilbert space that the potential spans.

5 Outlook

For further investigations in comparing these potentials, I would recommend performing scattering cross section analysis. By calculating the resulting scattering cross section from the potentials and comparing them to experimental data as well as to each other, it would become more clearly visible how the different potentials model the interaction between neutron and nucleus. It would also be recommended to represent potentials for protons as well as neutrons scattering of other nuclei in the same way and determine if it is feasible to create a global analytical representation of the microscopic model potential. Also consider other potential forms such as [13] and study the impact of deformation for example using the potential model in development in Lund [14, 15].

References

[1] C Hebborn and F M Nunes et al. Optical potentials for the rare-isotope beam era. *Journal of Physics G: Nuclear and Particle Physics*, 50(6):060501, 2023.

[2] Calvin W Johnson and Kristina D Launey et al. White paper: from bound states to the continuum. *Journal of Physics G: Nuclear and Particle Physics*, 47(12):123001, 2020.

[3] A.J. Koning and J.P. Delaroche. New neutron and proton optical models. *International Nuclear Data Committee(Nuclear Data Science)*, 431:55–76, 2002.

[4] F. Perey and B. Buck. A non-local potential model for the scattering of neutrons by nuclei. *Nuclear Physics*, 32:353–380, 1961.

[5] A. Idini, C. Barbieri, and P. Navrátil. Ab initio optical potentials and nucleon scattering on medium mass nuclei. *Physical Review Letters*, 123(9):092501, 2019.

[6] I.J. Thompson and F. M. Nunes. *Nuclear reactions for astrophysics: principles, calculation and applications of low-energy reactions.* Cambridge University Press, 2009.

[7] E. Amsler. *Scattering in Quantum Mechanics: Cross Section Calculations.* CERN, 2008.

[8] K. Hagino, K. Ogata, and A.M. Moro. Coupled-channels calculations for nuclear reactions: From exotic nuclei to superheavy elements. *Progress in Particle and Nuclear Physics*, 125, 2022.

[9] P.E. Hodgson. The nuclear optical model introductory overview. In *Nucleon-nucleus optical model up to 200 MeV. Proceedings of a specialist meeting*, 1997.

[10] A.J. Koning and J.P. Delaroche. Local and global nucleon optical models from 1 kev to 200 mev. *Nuclear Physics A*, 713(3-4):231–310, 2003.

[11] Yuan Tian, Dan-Yang Pang, and Zhong-Yu Ma. Systematic nonlocal optical model potential for nucleons. *International Journal of Modern Physics E*, 24(01):1550006, 2015.

[12] Herman Feshbach. Unified theory of nuclear reactions. *Annals of Physics*, 5(4):357–390, 1958.

[13] M. Burrows, K. D. Launey, A. Mercenne, R. B. Baker, G. H. Sargsyan, T. Dytrych, and D. Langr. Ab initio translationally invariant nucleon-nucleus optical potentials. *Phys. Rev. C*, 109:014616, 2024.

[14] A Idini, J Rotureau, J Boström, J Ljungberg, and B G Carlsson. Towards microscopic optical potentials in deformed nuclei. *Journal of Physics: Conference Series*, 2586(1):012049, 2023.

[15] J. Ljungberg, B. G. Carlsson, J. Rotureau, A. Idini, and I. Ragnarsson. Nuclear spectra from low-energy interactions. *Phys. Rev. C*, 106:014314, Jul 2022.